Article

Fluid Infiltration and Mass Transfer along a Lamprophyre Dyke–Marble Contact: An Example from the South-Western Korean Peninsula

Jungrae Noh [1], Changyeob Kim [1], Vinod O. Samuel [1],*, Yirang Jang [2], Seung-Ik Park [3] and Sanghoon Kwon [1]

[1] Department of Earth System Sciences, Yonsei University, Seoul 03722, Korea; jrnoh@yonsei.ac.kr (J.N.); kcy0202@yonsei.ac.kr (C.K.); skwon@yonsei.ac.kr (S.K.)

[2] Department of Earth and Environmental Sciences, Chonnam National University, Gwangju 61186, Korea; yirangjang@gmail.com

[3] Department of Geology, Kyungpook National University, Daegu 41566, Korea; psi@knu.ac.kr

* Correspondence: vosamuel@gmail.com

check for updates

Abstract: In this contribution, we report the metasomatic characteristics of a lamprophyre dyke–marble contact zone from the Hongseong–Imjingang belt along the western Gyeonggi Massif, South Korea. The lamprophyre dyke intruded into the dolomitic marble, forming a serpentinized contact zone. The zone consists of olivine, serpentine, calcite, dolomite, biotite, spinel, and hematite. Minor F and Cl contents in the serpentine and biotite indicate the composition of the infiltrating H_2O-CO_2 fluid. SiO_2 (12.42 wt %), FeO (1.83 wt %), K_2O (0.03 wt %), Sr (89 ppm), U (0.7 ppm), Th (1.44 ppm), and rare earth elements (REEs) are highly mobile, while Zr, Cr, and Ba are moderately mobile in the fluid. Phase equilibria modelling suggests that the olivine, spinel, biotite, and calcite assemblage might be formed by the dissolution of dolomite at ~700 °C, 130 MPa. Such modelling requires stable diopside in the observed conditions in the presence of silica-saturated fluid. The lack of diopside in the metasomatized region is due to the high K activity of the fluid. Our log activity K_2O (a_{K2O})–temperature pseudosection shows that at a_{K2O}~−40, the olivine, spinel, biotite, and calcite assemblage is stable without diopside. Subsequently, at ~450 °C, 130 MPa, serpentine is formed due to the infiltration of H_2O during the cooling of the lamprophyre dyke. This suggests that hot H_2O-CO_2 fluids with dissolved major and trace elements infiltrated through fractures, grain boundaries, and micron-scale porosity, which dissolved dolomite in the marble and precipitated the observed olivine-bearing peak metasomatic assemblage. During cooling, exsolved CO_2 could increase the water activity to stabilize the serpentine. Our example implies that dissolution-reprecipitation is an important process, locally and regionally, that could impart important textural and geochemical variations in metasomatized rocks.

Keywords: dyke–marble contact; metasomatism; dissolution-precipitation; phase equilibria; H_2O-CO_2 fluid; K activity

1. Introduction

Metasomatism is the alteration of rocks by hot, chemically active fluids that infiltrate or diffuse through the rocks, causing recrystallization and compositional change [1]. Heat and fluids released by the crystallizing magma could pervasively interact with the rocks regionally or locally, generating metasomatized zones/aureoles [2,3]. On a regional scale, infiltration by H_2O-CO_2 brines causes metasomatic alterations in the lower crust and the mantle [4–6]. During metasomatic alteration, metal concentrations in fluids can lead to the genesis of ore deposits that are economically important [7].

Significant changes in mineralogy, geochemistry, and rheology evolved through fluid–rock interactions are important in evaluating geodynamic processes over time [8]. Metasomatic changes through the introduction of fluid from an external source adds and removes materials in solution by infiltration metasomatism [9,10]. The chemical potential of perfectly mobile components depends not only on their concentration but also on the influence of inert (immobile) components in the system during the infiltration metasomatism, where the chemical potentials of perfectly mobile components differ from those in the external medium in contrast to diffusion processes [9]. Our understanding of such processes is limited because of the lack of fluid properties under high pressure (P) and temperature (T) conditions, and the absence of fluid phase preserved in these samples. Important advances are made by the constraining of our understanding of fluid properties [11]. Further textural and geochemical studies of metasomatic zones are very useful in understanding metasomatism and the dissolution-precipitation process, and can deliver more information about the chemical composition of fluids and mobility of different components in it with respect to the external conditions [12].

Our understanding about metasomatism in natural systems comes from outcrop-scale observations of such phenomena due to magmatism in rocks [13–17]. The metasomatism of marble attracted wide attention because of sharp changes in mineralogy between metasomatized and unmetasomatized sections compared to metasomatized igneous or other metamorphic rocks [13–15]. A simple chemical system includes the formation of metasomatic products and their well-defined thermodynamic properties [13]. Such metasomatized zones in marble are commonly characterized by the replacement of dolomite by olivine. The formation of the infiltration-driven olivine-bearing metasomatic zone by the silicification of dolomite could be represented by the following Reaction [13]:

$$\text{Dolomite} + \text{SiO}_2 \text{ (aq)} = \text{Forsterite} + 2\text{Calcite} + 2\text{CO}_2. \tag{1}$$

Nevertheless, the Equation (1) requires an aqueous fluid with an activity of SiO_2 of less than one in order to form forsterite at the observed pressure (P) and temperature (T) conditions [14–20]. In silica-saturated fluids, forsterite cannot be formed by a direct reaction between dolomite and silica-saturated fluid [13]. If fluid is silica-saturated, forsterite can be formed by Equation (2), where the initial silica activity is reduced by the formation of diopside [21–26].

$$\text{Diopside} + 3\text{Dolomite} = 2\text{Forsterite} + 4\text{Calcite} + 2\text{CO}_2. \tag{2}$$

Several other possibilities have been proposed for the formation of forsterite during the contact metamorphism of carbonate rocks, suggesting that metasomatic olivine in dolomitic marble could be a source of silica other than diopside if the reaction occurred far from equilibrium/disequilibrium [25–28]. Here, we investigate an infiltration metasomatic zone developed on a dolomitic marble by lamprophyre dyke intrusion. The formation of an olivine-bearing serpentinized metasomatic zone developed on dolomitic marble is examined through textural study, geochemical information, and phase equilibria modelling. We also provide geochemical variation in elements, which might be an important factor in characterizing the mobility of different elements during such an infiltration process. Thus, the main objective of this study is to expand our understanding of geochemical variations during infiltration metasomatism by taking an example of metasomatism caused by a lamprophyre dyke–marble contact zone from the southwestern Korean Peninsula.

2. Geological Setting and Sampling

In the southwestern Korean Peninsula, the Hongseong-Imjingang belt (Figure 1), which is also called the Gyeonggi marginal belt [29], along the western Gyeonggi Massif has been considered as part of the most plausible collisional belt in the Korean Peninsula. The belt is correlated to the Qinling-Dabie-Sulu belt between the North and South China cratons in terms of collisional tectonics [30–43]. Our samples are from a lamprophyre dyke–marble contact zone exposed in the southern part of the Hongseong-Imjingang belt. Such dykes (predominantly quartz porphyry,

lamprophyre, andesite, and felsite) in the study area are reported to have formed mostly in the Jurassic times [44]. Lamprophyre dykes are considered as a tectonic marker of late orogenic transtension [45].
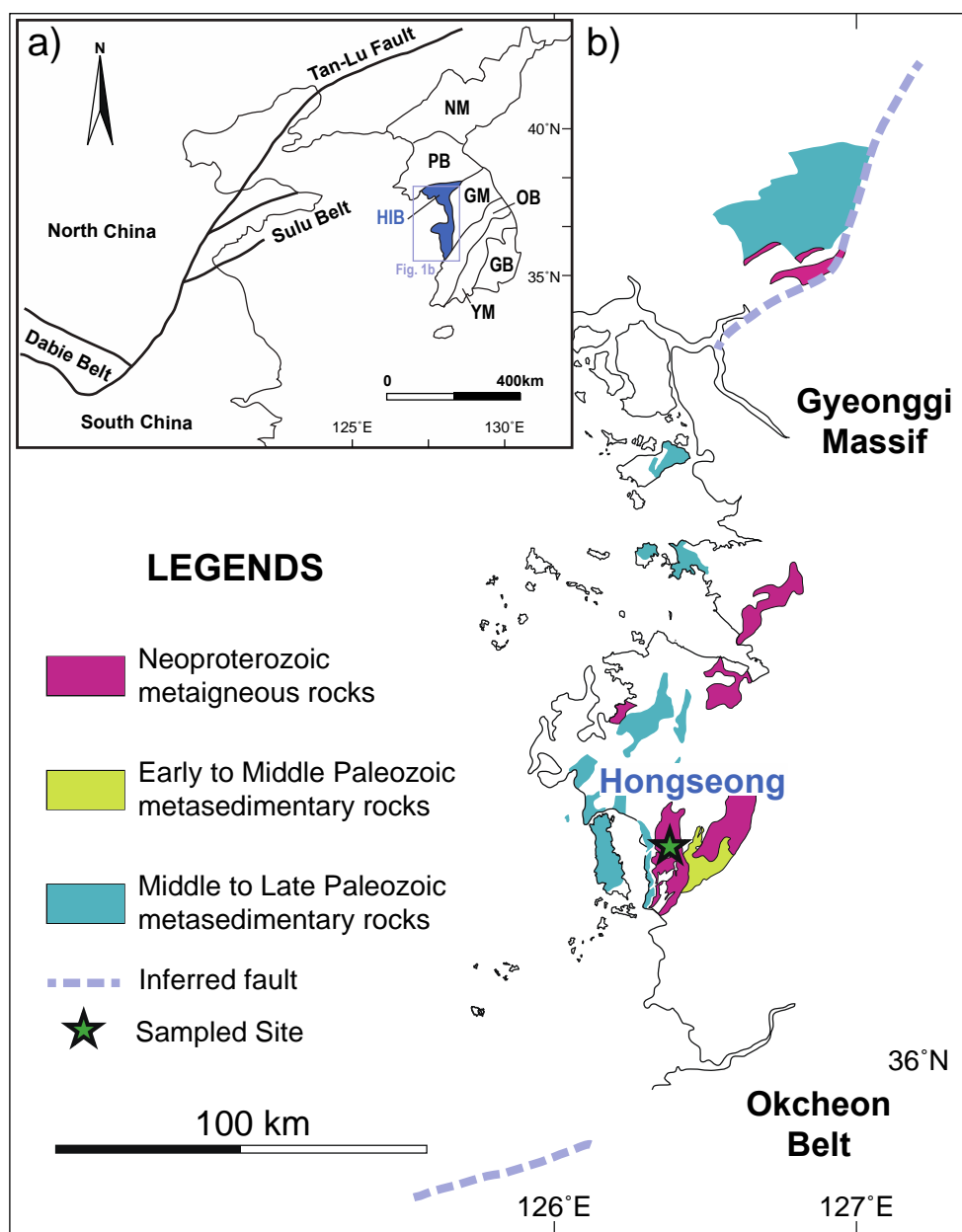
Figure 1. (**a**) Simplified tectonic map of East Asia. (**b**) Geologic map of the western part of the Korean Peninsula, showing the location of the lamprophyre dyke–marble contact zone (modified form [30] and references therein).

The medium-grained dark-colored ~1 m-width lamprophyre dyke intruded the dolomitic marble of ~10 m exposure. The dyke consists of dark to brown biotite and amphibole crystals of ~2 to 5 mm in size, indicating a relatively slow cooling during their crystallization because of insulation by the surrounding marble. The light-greenish ~70 cm-width metasomatic area is formed within the marble along the dyke–marble contact (Figure 2a). This area displays well-defined mineralogical zones with a light greenish to dark-colored highly serpentinized area and light brownish-colored partially serpentinized olivine-bearing portions (Figure 2b). The serpentinized area is relatively fine-grained (<1 mm) compared to the medium-grained (2–3 mm) olivine-bearing portions. As we move further

towards the unmetasomatized marble region, there are alternating mm-scale thin layers of olivine and calcite that could have been formed by the self-organization of minerals driven by grain growth (Figure 2b) [46].
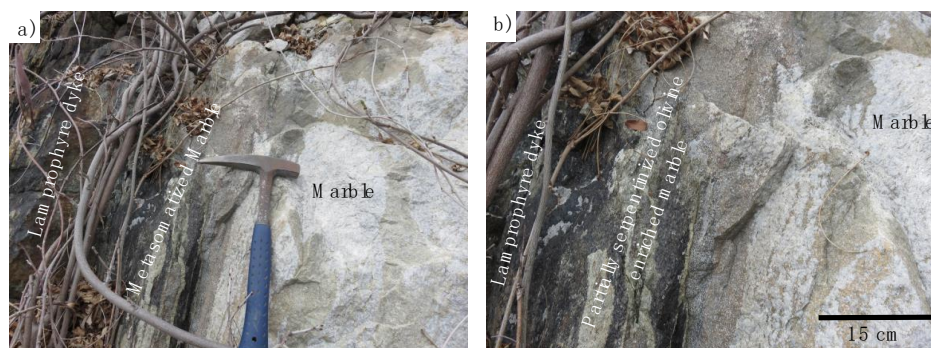
Figure 2. Representative field photos of the lamprophyre dyke–marble contact from the south-western Korean Peninsula in the Hongseong-Imjingang belt. (**a**) Light greenish metasomatized region at the contact zone. (**b**) Enlarged photo of the contact zone showing a light greenish to light brownish partially serpentinized olivine-enriched region. The highly serpentinized area (with minor olivine) is relatively fine-grained and appears dark compared to the medium-grained olivine-bearing portions.

A total of nine samples were systematically collected from a road-cut outcrop, exposing a metasomatized zone comprising a lamprophyre dyke ~1 m in width (Figure 3). Three samples of lamprophyre dyke were collected from this dyke at distances 0.5 m apart (Figure 3a). We avoided sampling close to the contact zone in order to obtain the original composition of the lamprophyre dyke. Three olivine-bearing samples (0.5 m apart from one another) were also collected from the partially serpentinized, olivine-enriched area (Figure 3b). Again, three marble samples were collected, 0.5 m apart, ~1 m away from the metasomatized region (Figure 3c). From these samples, petrographic observation was carried out on thin sections to investigate the changes in mineralogy and bulk rock chemistry during the metasomatic processes. Because of the consistency in the mineral assemblage of each group, one sample from each group is considered representative for the further investigation using both the electron microprobe and bulk rock chemistry to assess the variations in mineral chemistry as well as the major, trace, and rare earth element (REE) abundances, respectively.
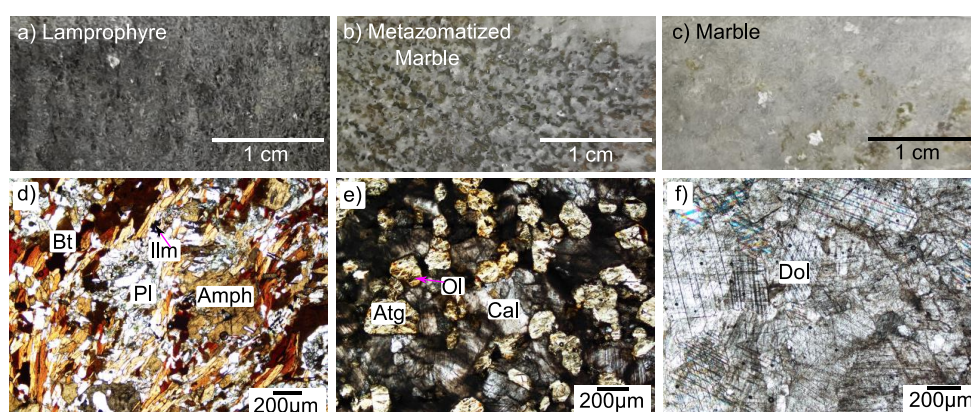

Figure 3. Hand specimens and thin section photographs of the three representative samples collected for this study. (**a**) Dark, medium-grained lamprophyre dyke sample. (**b**) Olivine-bearing sample from the partially serpentinized area. (**c**) Marble sample collected away from the metasomatized area. Scale given for panel c is same for all panels. (**d**–**f**) Thin section photographs of lamprophyre dyke, metasomatized marble, and dolomitic marble, respectively. Bt—Biotite; Ilm—Ilmenite; Pl—Plagioclase; Amph—Amphibole; Atg—Antigorite; Ol—Olivine; Cal—Calcite; Dol—Dolomite.

## 3. Petrography

3.1. Lamprophyre

All the three lamprophyre samples are mineralogically similar and show minor grain size variations. The lamprophyre sample consists mainly of amphibole, biotite, and plagioclase (Figure 3a,d and Figure 4). Biotite and amphibole are present in similar amounts and constitute most of the sample (Figure 4a). Plagioclase covers ~20% of the sample. A minor amount (1–2%) of quartz is present occasionally. Biotite appears as mm-size, elongated laths, and is mainly present as a group of three to four laths. The amphibole shape is wider and bigger compared to biotite. It also exists as a group of grains in the plagioclase matrix. Few amphiboles have apatite inclusions (Figure 4b) that are not observed in the matrix. Plagioclase forms subhedral grains that are mostly interconnected. The major opaque mineral is ilmenite, and it is present dispersed in the matrix, as inclusions, and as discrete grains on the grain boundaries of amphibole and biotite.
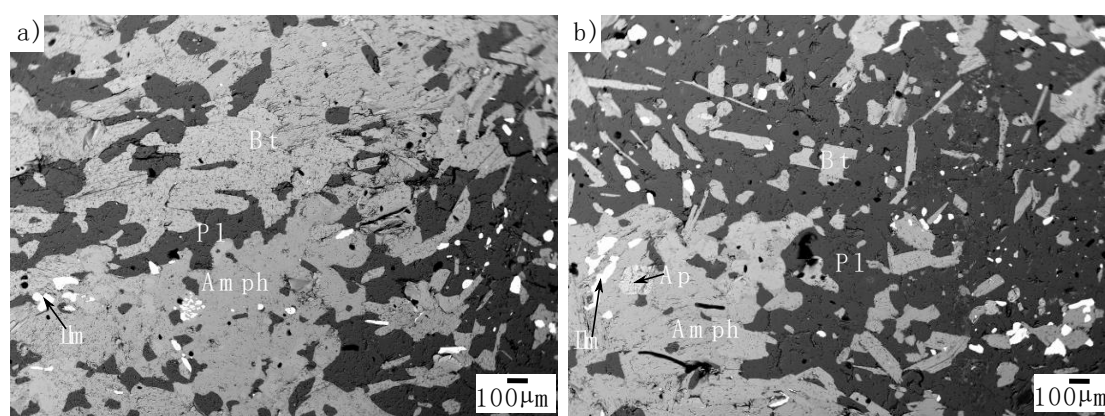
Figure 4. Back-Scattered Electron (BSE) images of the lamprophyre dyke sample, showing the biotite, amphibole, plagioclase, and ilmenite assemblage (**a**), and the biotite, amphibole, plagioclase, and ilmenite assemblage with apatite inclusions in amphibole (**b**). Bt—Biotite; Ilm—Ilmenite; Pl—Plagioclase; Amph—Amphibole; Ap—Apatite.

### 3.2. Metasomatized Intermediate Marble

Three intermediate metasomatized partially serpentinized marble samples consist of dolomite, calcite, olivine, serpentine (antigorite), biotite, spinel, and hematite (Figure 3b,e and Figure 5). Most of the dolomite has a resorbed texture with an irregular boundary. They are mostly replaced by calcite and serpentine in a large area in the metasomatized thin section (Figure 5a). Serpentinization appears as large pods in association with calcite and minorly resorbed dolomite. Few olivine grains are preserved within the serpentinized pods with resorbed olivine in them (Figure 5b). They might be former olivine grains that were replaced during a later hydration event. Only two biotite grains are observed in the entire thin section (Figure 5c). They appear along the contact between the calcite and serpentinized pods. Biotite has a thick blade-like texture compared to the elongated ones in the lamprophyre. Minor euhedral spinel is present along the dolomite–calcite contact (Figure 5d). The major oxide mineral is hematite, and Ti is absent. It is easily distinguished by their polished surface compared to the rough surface that is commonly observed in magnetite. Hematite forms as micro-meter-sized grains dispersed along the grain boundaries of serpentinized pods (Figure 5e). They appear like the oxidation texture formed on earlier olivine grains. They are also present as veins and discrete grains, well-dispersed in the calcite dolomite matrix. Replacement calcite precipitation also occurs along the cleavage planes of dolomite grains (Figure 5f).
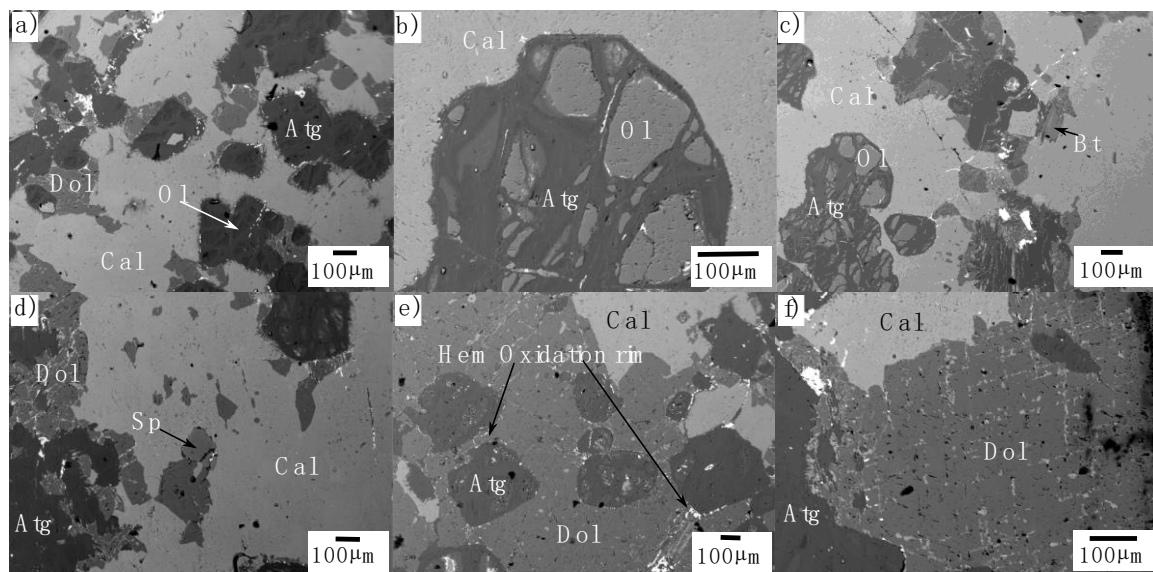
Figure 5. Back-Scattered Electron (BSE) images of an intermediate metasomatized sample, showing dolomite dissolution to form olivine, calcite, and serpentine (**a**); resorbed olivine grains within the serpentinized pods (**b**); biotite present along with the serpentinized olivine-bearing pods, calcite, and dolomite assemblage (**c**); euhedral spinel present along the dolomite and calcite contact (**d**); hematite forms as micrometer-sized grains dispersed along the grain boundaries of the serpentinized pods, as veins and as discrete grains (**e**); replacement calcite precipitation along the cleavage planes of dolomite grains (**f**). Bt—Biotite; Ilm—Ilmenite; Pl—Plagioclase; Amph—Amphibole; Atg—Antigorite; Ol—Olivine; Cal—Calcite; Dol—Dolomite; Sp—Spinel.

3.3. Marble

All the three marble samples consist mostly of dolomite (Figure 3c,f and Figure 6). Near the contact zone, where metasomatism occurred, veins of serpentine and calcite were formed in the dolomitic marble (Figure 6). Here, both a serpentine vein with precipitated calcite (Figure 6a) and a calcite vein with precipitated serpentine (Figure 6b) occur simultaneously, in all three samples. There are no calcite grains observed in the marble sample other than those created in the vein filling fractures.
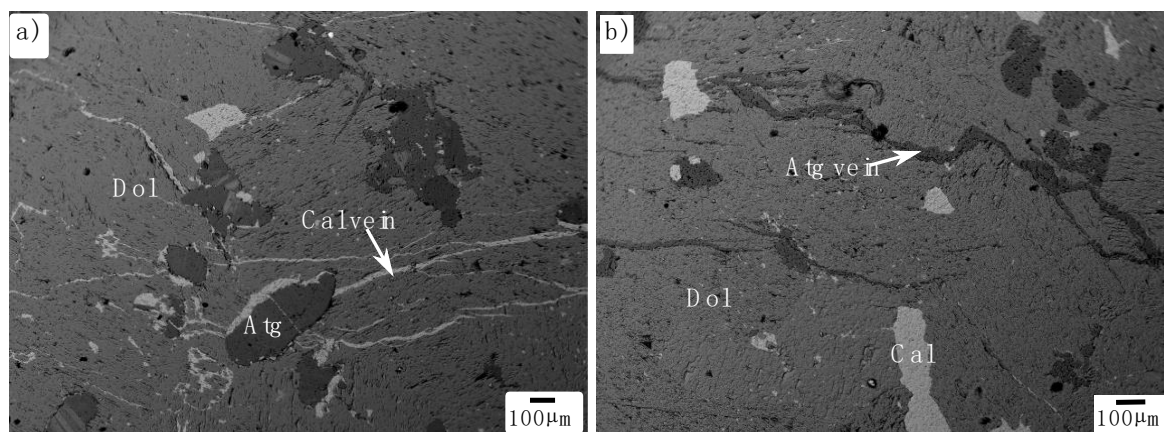
Figure 6. Back-Scattered Electron (BSE) images of the dolomitic marble sample, showing calcite veins and serpentine precipitation in the dolomitic matrix (**a**), and serpentine veins and calcite precipitation in the dolomitic matrix (**b**). Dol—Dolomite; Cal—Calcite; Atg—Antigorite.

4. Analytical Techniques

4.1. Electron Probe Micro Analyzer (EPMA)

The mineral compositions of three representative samples of the lamprophyre dyke, the intermediate metasomatized zone, and the dolomitic marble were analyzed using a JEOL JXA-8100 Superprobe, Electron Probe Micro Analyzer (EPMA), housed at the Earth System Sciences, Yonsei University, Seoul, Korea. Analyses were performed using an accelerating voltage of 20 kV, beam current of 20 nA, and counting time of 10 s. Care has been taken to analyze mineral core compositions in order to obtain compositions that might be present during peak crystallization/metasomatic conditions. An electron beam spot size of 5 μm is used for the analysis of biotite, amphibole, ilmenite, olivine, serpentine, calcite, dolomite, spinel, and hematite and 15 μm for plagioclase. Natural and synthetic silicates and oxides supplied by JEOL and ASTIMEX standards Ltd. (Saint-Hubert, QC, Canada), were used for calibration. The data were reduced using the ZAF correction procedures supplied by JEOL. Apatite standardization and offline interference corrections have been carried out based on suggestions from [47]. An electron beam spot size of 15 μm is used for the apatite analysis. The standards for apatite and REEs are generously provided by Dr. Daniel Harlov, GFZ, Postdam, Germany.

4.2. Bulk Chemistry

A whole-rock analysis of three representative samples of the lamprophyre, the intermediate metasomatized zone, and the dolomitic marble were carried out for the major, trace, and rare earth element (REE) abundances at Activation Laboratories, Ltd., Ancaster, ON, Canada. The lithium metaborate/tetraborate fusion ICP method was used for the major and trace elements. Samples were run for major oxides and selected trace elements on a combination simultaneous/sequential Thermo Jarrell-Ash ENVIRO II ICP or a Varian Vista 735 ICP. Calibration was performed using 14 prepared USGS and CANMET-certified reference materials. One of the 14 standards was used during the analysis for every group of 10 samples. Totals should be between 98.5% and 101%. If the results came out lower, the samples were scanned for base metals. Low reported totals may indicate sulphate being present or other elements such as Li, which would not normally be scanned for. Samples with low totals, however, were automatically re-fused and reanalyzed. Option 4B1 was used for accurate levels of the base metals Cu, Pb, Zn, Ni, and Ag. In-lab standards (traceable to certified reference materials) or certified reference materials were used for quality control. Samples were analyzed using a Varian Vista 735 ICP. Option 4B-INAA (Instrumental Neutron Activation Analysis) for the As, Sb, high W > 100 ppm, Cr > 1000 ppm, and Sn > 50 ppm (for details, please visit https://actlabs.com/geochemistry/lithogeochemistry-and-whole rock analysis/).

5. Results

5.1. Mineral Chemistry

5.1.1. Lamprophyre Dyke

Primary minerals analyzed in the lamprophyre dyke include biotite, amphibole, plagioclase, ilmenite, and apatite (Supplementary Materials Table S1). Here, biotite and amphibole have higher TiO_2 contents of 4.7–5 wt % and 2.1–2.4 wt %, respectively. The F and Cl values of biotite range from 0.0 to 0.14 and 0.04 to 0.07, respectively. In the amphibole, the F and Cl values range from 0.0 to 0.48 and 0.01 to 0.05, respectively. Mineral compositions show that biotite has $X_{Mg} = 0.41$–0.42, amphibole has $X_{Mg} = 0.45$–0.52, and plagioclase has $X_{An} = 0.30$–0.33. Most of the amphiboles are pargasitic, but one has hornblende in its composition. Ilmenite ($X_{Ilm} = 0.97$–0.98) contains minor pyrophanite ($X_{Pyr} = 0.02$). The F and Cl values of apatite range from 2.04 to 3.71 and 0.13, respectively. The chondrite normalized REE values in apatite show a slight enrichment in the HREE.

### 5.1.2. Metasomatized Intermediate Marble

Olivine, serpentine (antigorite), spinel, biotite, calcite, dolomite, and hematite are analyzed from the metasomatized intermediate marble sample (Supplementary Materials Table S2). Olivine composition has X_{Mg} = 0.94 with 5–7 wt % FeO in them. The F and Cl values of serpentine and biotite are negligible (~0.01 wt %). Serpentine has X_{Mg} = 0.94 with 1–4 wt % FeO. It is identified as antigorite based on its non-fibrous texture and has both FeO and MgO content in it. Biotite has a phlogopite composition with X_{Mg} = 0.94–0.95. Spinel has X_{Mg} = 0.86, X_{Fe} = 0.14, and X_{Cr} = 0.007. Hematite has a 0.003 X_{Cr} component. Dolomite consists of ~21 wt % MgO and ~31 wt % CaO, with minor FeO ~0.9 wt %. Calcite has ~54 wt % CaO, with minor MgO (~3 wt %) and FeO (~0.3 wt %).

5.1.3. Marble

Serpentine, calcite, and dolomite are analyzed in the marble sample (Supplementary Materials Table S3). Serpentine has X_{Mg} = 0.99, with a very small content of FeO (~0.97 wt %) compared to that in the metasomatized zone. In the serpentine, the F and Cl values are ~0.3 wt % and ~0.01 wt %, respectively. Calcite has ~52 wt % CaO, with a small amount of MgO (~1.38 wt %) and FeO (~0.04 wt %) compared to the metasomatized zone. Dolomite consists of ~20 wt % MgO and ~30 wt % CaO with minor FeO ~0.15 wt %.

5.2. Bulk Chemistry

The bulk chemistry results of the representative samples of lamprophyre dyke, the metasomatized intermediate marble, and the marble are given as Supplementary Materials Table S4. The lamprophyre dyke has an SiO_2 content of 49.19 wt % and a total $CaO + Na_2O + K_2O$ content of 11.62 wt %. Both marble and metasomatized marble has a CaO of 30–31 wt % and MgO of 18–20 wt %. Metasomatized marble is comparatively enriched in SiO_2 (14.67 wt %), FeO (2.13 wt %), and K_2O (0.3 wt %) compared to the marble (Figure 7a–c; Supplementary Materials Table S4).
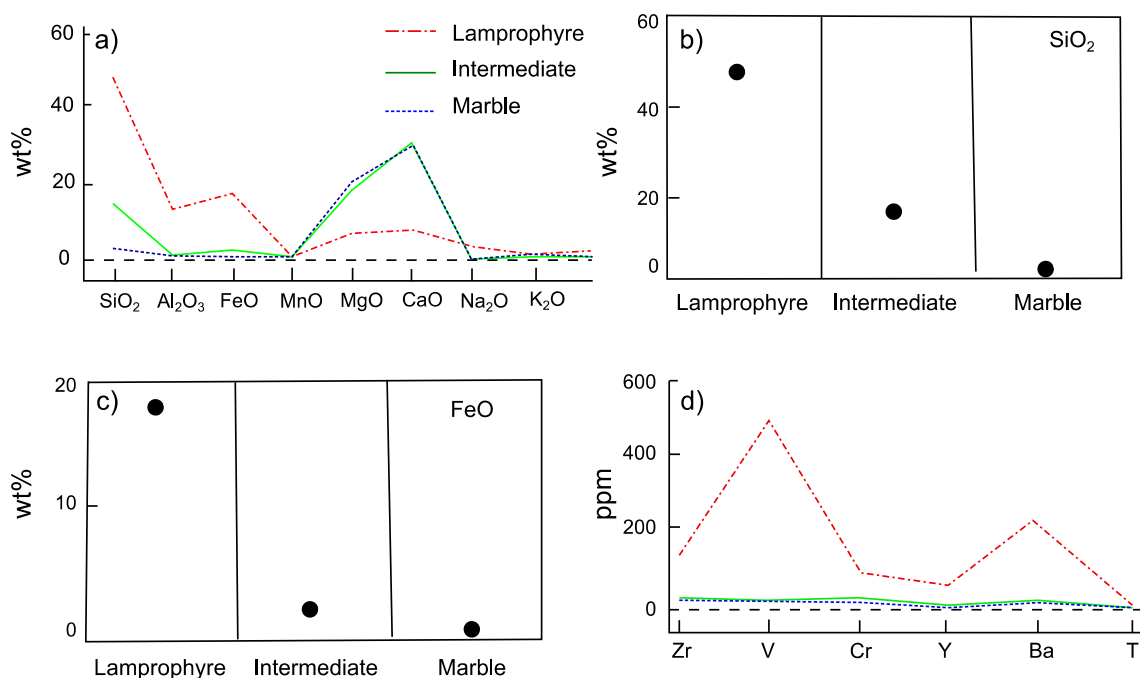
Figure 7. Geochemical enrichment of major elements as well as moderately enriched elements during metasomatism. Compositional diagrams showing the SiO_2 and FeO enrichment (wt %) in the metasomatized marble (**a**), Major element variations (wt %) (**b**), SiO_2 variation (wt %) (**c**), FeO variation (wt %), and (**d**), moderately enriched elements variation from the representative samples (ppm).

Trace element composition of the representative samples are divided into three groups based on their enrichment in the metasomatized marble compared to the marble (Supplementary Materials Table S4). Zr, V, Cr, Y, Ba, LREE, Sr, U, and Th are enriched in the metasomatized marble compared to the marble (Figure 7d; Figure 8a–c). Among the elements, Zr, V, Cr, Y, and Ba are moderately enriched, and have values less than that of the lamprophyre dyke (Figure 7d). The primitive mantle normalized REE values [48] show that they are high in the lamprophyre dyke compared to the marble (Figure 8a). The REE pattern shows that LREEs are comparatively depleted compared to HREEs in the dyke sample (Figure 8a). LREEs in the marble are slightly enriched compared to HREEs (Figure 8a). In the metasomatized marble, LREEs are highly enriched, and HREEs show a flat pattern comparable to the marble (Figure 8a).
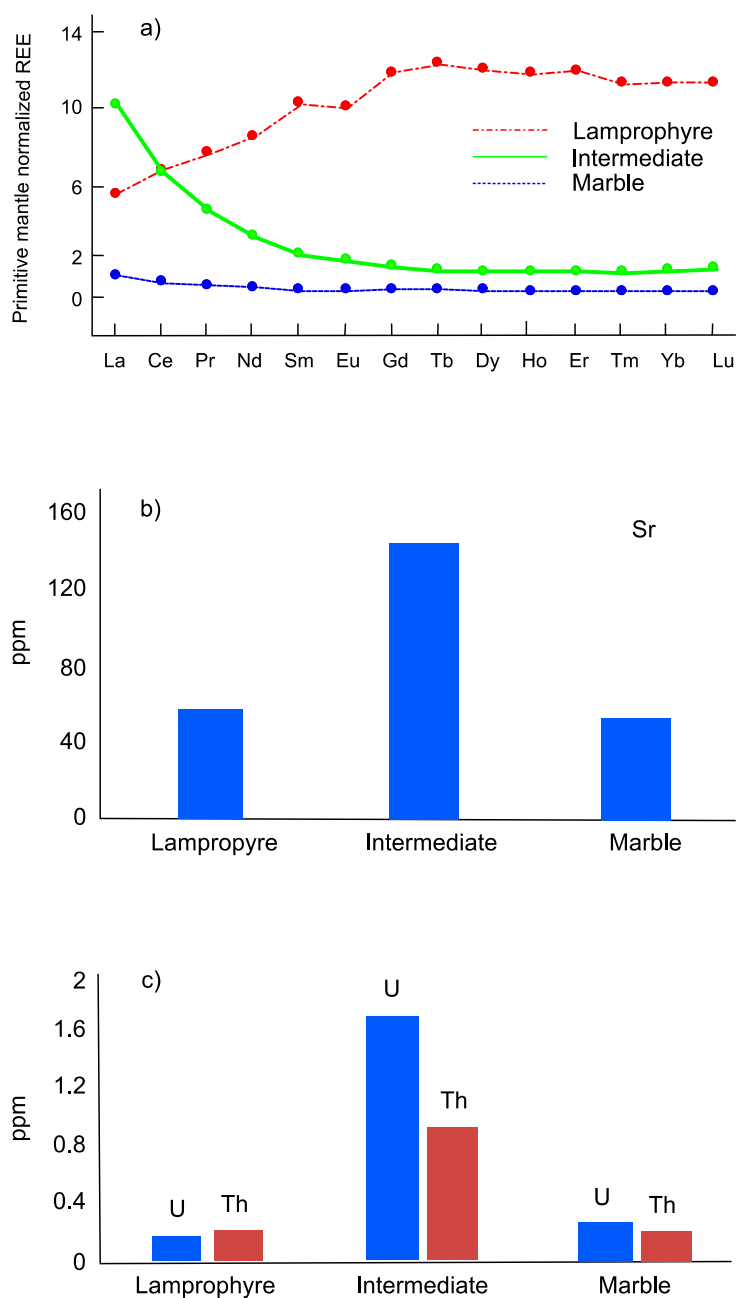
Figure 8. Geochemical enrichment of trace elements during metasomatism. (**a**), Primitive mantle normalized REE diagram (**b**), Sr variation (**c**), U and Th variation from the representative samples.

The Sr, U, and Th in the metasomatized marble are very high compared to both the lamprophyre dyke and the marble (Figure 8b). There are no other elements except these three elements that show such a high enrichment compared to the other two samples. Among the elements, Sr shows the highest enrichment of ~600 ppm, and U and Th are moderately enriched. Most of the other analyzed elements such as Be, Rb, Ni, Cu, Zn, Ag, Nb, Ta, W, Pb, Ge, Sc, Co, Ga, Cs, and Hf have high contents in the lamprophyre dyke. These elements are not particularly enriched in the metasomatized marble. All these elements have comparatively similar values in both the metasomatized and the un-metasomatized portions of the marble.

5.3. Phase Equilibria Modelling

The petrologic pseudo-sections were computed using PERPLE_X 6.7.9 version available at http://www.perplex.ethz.ch [49–51] using the hp02ver.dat database [52]. An H_2O-CO_2 fluid equation of state [53] is used to model these phase diagrams. The bulk chemistry data of the intermediate metasomatized marble (Supplementary Materials Table S4) is used for the modelling. The P_2O_5, Na_2O, and TiO_2 concentrations were not considered due to their low contents (<0.5 wt %). The total loss on ignition (LOI) in this sample is 32.88. The H_2O content is assumed to be 0.1% of this total LOI. The value of CO_2 is 30.25 wt % and of H_2O is 2.5 wt %. The solid solution models used for the modelling are olivine (O(HP)) [52], serpentine (Atg; ideal), calcite (Cc(AE)) [54], dolomite (Do(HP)) [52], biotite (Bio(TCC)) [55], and spinel (Sp(HP)) [52].

In the first calculation, we attempted to vary the pressure (P) between 30 and 200 MPa and temperature (T) between 300 and 800 °C. The result shows that olivine, diopside, dolomite, calcite, and CO_2 are stable in this window, where the dolomite to calcite transition occurs above 500 to 650 °C (Figure 9a). We have not observed any diopside in our sample. In addition, we have not observed stable biotite or serpentine in the phase diagram at the first attempt.
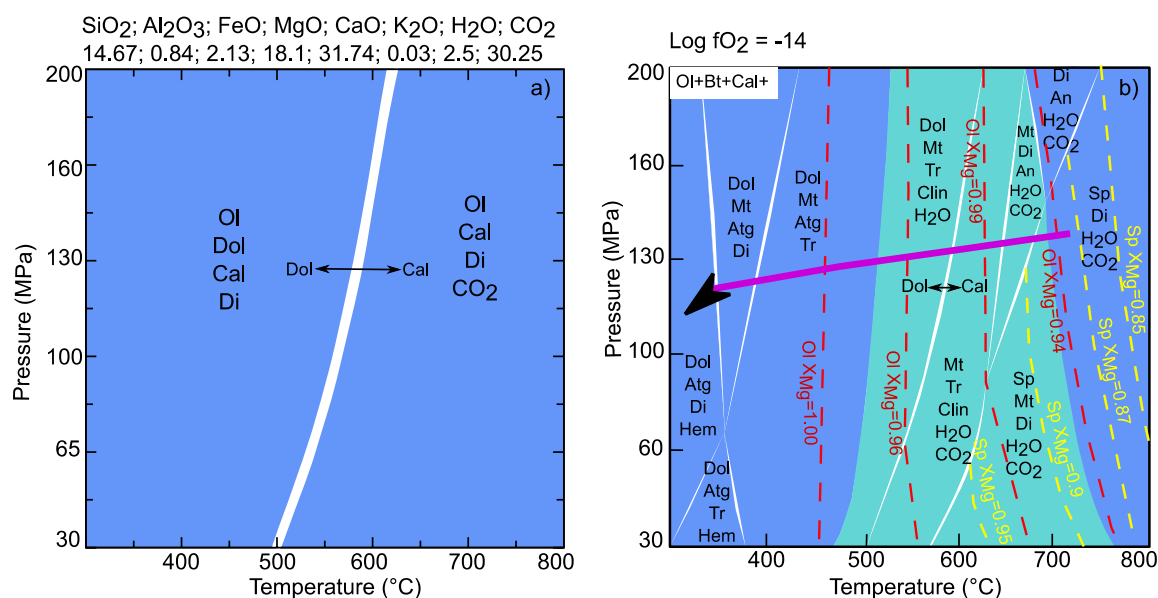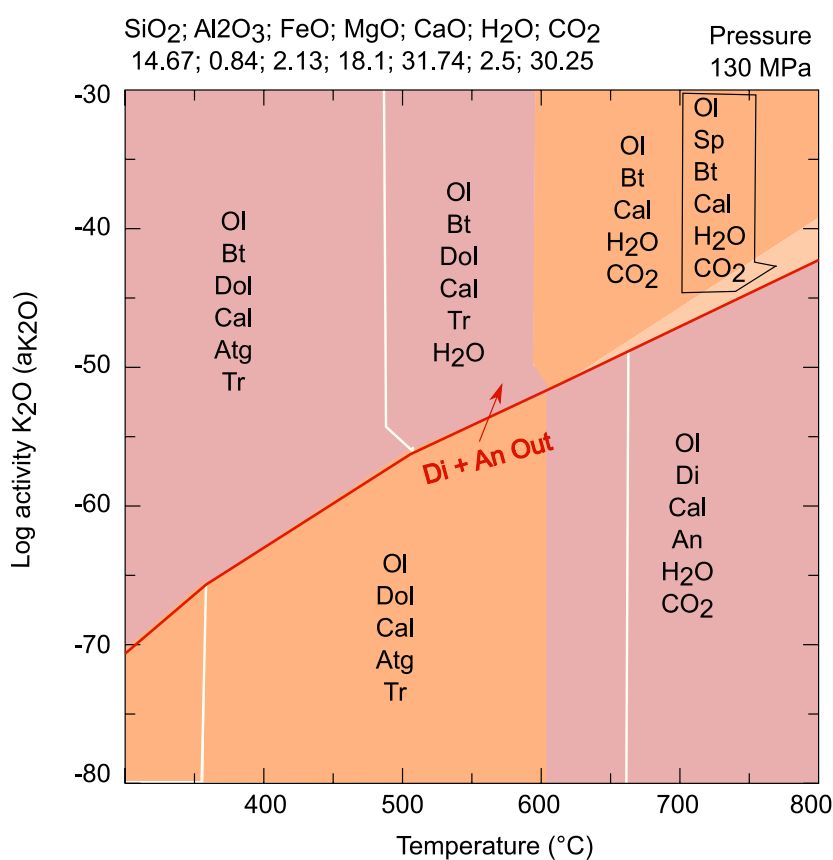

Figure 9. Pseudosection calculations showing stable minerals at different conditions. Bulk chemistry used for the calculation is given above the diagram. (**a**) The results with varying pressure and temperature from (**a**) 30 to 200 MPa and 300 to 800 °C and (**b**) 30 to 200 MPa and 300 to 800 °C at logfO_2 = −14. Pink arrow representing the possible evolutionary path followed by the metasomatized marble zone. Ol—Olivine; Dol—Dolomite; Cal—Calcite; Di—Diopside; Mt—Magnetite; Hem—Hematite; Atg—Antigorite; Tr—Tremolite; Clin—Chlorite; Sp—Spinel; An—Anorthite.

Because of the hematite that is present as oxidation rims on the serpentine pods, vein-filled fractures, and discrete grains, we assumed an oxygen fugacity of ~log fO_2 = −14 with a magnetite

to hematite transition at 600–800 °C [56] in the second run. This result is more comparable to our petrologic observation except for the stability of diopside (Figure 9b). The second run successfully generated olivine, serpentine, biotite, spinel, calcite, dolomite, and hematite. Here, olivine, biotite, and calcite are stable everywhere in the phase diagram. The mineral composition of olivine shows X_{Mg} = 0.94. We have computed the isopleths for the X_{Mg} variation in olivine in the phase diagram. Our isopleth calculation shows that the olivine X_{Mg} is increasing towards the lower temperature portion in the phase diagram. An X_{Mg} of 0.94 is present towards ~750 °C. Since we observed spinel in the sample, we have computed the isopleths for X_{Mg} variation in spinel as well in the phase diagram. Spinel in our sample has an X_{Mg} of 0.86. This composition is also present near ~750 °C. Above ~130 MPa, spinel is absent and anorthite is stable. Therefore, the phase diagram result suggests a maximum pressure of ~130 MPa. Serpentine and hematite are stable towards the low-temperature portion at ~450 °C. Now, the major question is why we could not get any diopside in our sample. Our phase diagram calculations suggest that diopside is stable in the pressure-temperature conditions considered for these calculations.

　　Since we neither have observed any diopside inclusions in olivine nor have seen any possibility of low silica activity at out-of-equilibrium conditions, the K_2O activity has changed during the third run. The absence of diopside at high concentration of K is shown by the experimental results on granodioritic samples [57,58]. Furthermore, we have observed stable biotite in our sample, which makes it possible to consider varying K_2O activity during the phase diagram modelling. We have varied the log activity of K_2O from −80 to −30, and the temperature from 300 to 800 °C, with a pressure of 130 MPa. The result shows that with a high K_2O activity and at ~750 °C, olivine, spinel, biotite, and calcite are stable without diopside (Figure 10). Diopside will present only below a log a_{K2O} > −40, and above this condition all the phases observed in the metasomatized zone are stable.

Figure 10. Log activity K_2O-temperature pseudosection calculated at a pressure of 130MPa. Bulk chemistry used for the calculation is given above the diagram.

5.4. Isocon Method

To evaluate the percentage of addition or subtraction of mobile elements during metasomatism, we have applied the isocon method [59,60]. The density of metasomatized and un-metasomatized marble is measured, using conventional methods by measuring the mass and volume of the samples. The density of the unmetasomatized and metasomatized samples is 2.75 g/cm^3 and 2.74 g/cm^3, respectively. This defines an isocon for the elements, as shown in the formula of Equation (3) below:

$$C^{MM} = 1.0036 \times C^{M}, \tag{3}$$

where C^{MM} is the concentration of oxide or element in the metasomatized sample and C^{M} is the concentration of oxide or element in the unmetasomatized sample. The percentage difference in the mobile elements or oxides from this isocon can be calculated using Equation (4):

$$\% \text{ difference} = (C^{MM} - C^{M})/C^{M} \times 100. \tag{4}$$

These values are given in the Supplementary Materials Table S5. The deviation of each oxide or element from the isocon is represented in Figure 11. In the major elements, SiO_2 (552%), FeO (610%), and TiO_2 (487%) show maximum enrichments (Figure 11a). Al_2O_3, MnO, and K_2O are moderately enriched (~200–300%). CaO, MgO, and Na_2O are the least mobile or depleted (−33–4%) (Figure 11b). All the REEs are highly enriched in the metasomatized marble sample (>400%) (Figure 11c,d). Trace elements such as Th (576%), Cs (400%), Y (361%), U (304%), V (220%), Sr (167%), Zr (125%), Ba, and Nb (100%), and Cr (50%) also show a high enrichment compared to the unaltered sample (Figure 11c,d).
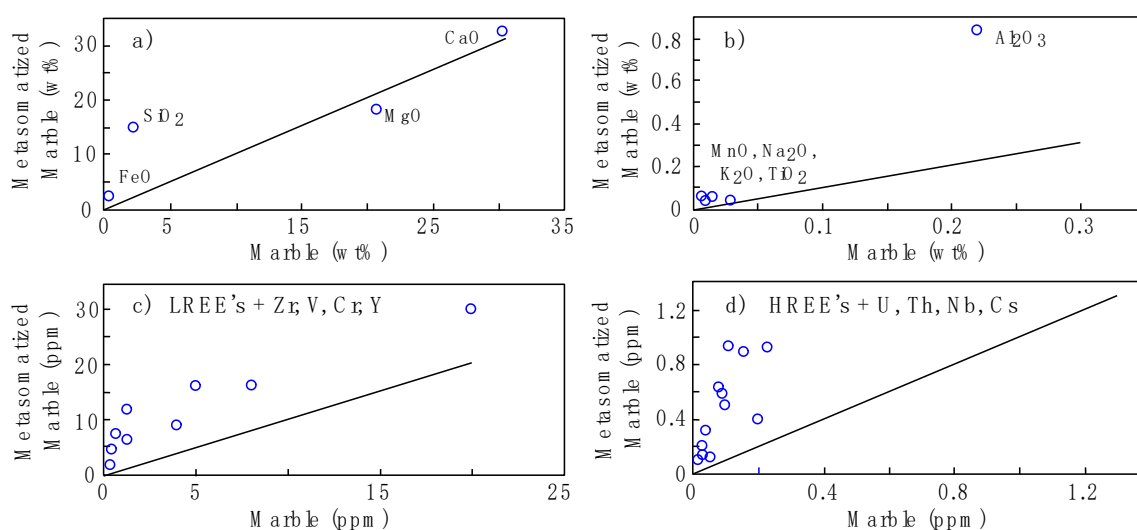
Figure 11. Deviation of major and trace elements and REEs from the isocon (straight line). (**a**) Deviation of SiO_2, FeO, MgO, CaO; (**b**) Deviation of Al_2O_3, MnO, Na_2O, K_2O, TiO_2; (**c**) Deviation of LREE's and Zr, V, Cr, Y ; (**d**) Deviation of HREE's and U, Th, Nb, Cs.

6. Discussion

The intrusion of hot magma into country rocks is a common phenomenon, and is important in understanding the process of the exchange of heat and fluids between cooling magma and cold country rocks [16,17,61–63]. Fluid infiltration and heating around the boundaries of a hot magmatic intrusion cause chemical and mineralogical alterations to nearby rocks [15–17,27]. Such altered rocks are typically called skarn [61–66]. Different types of rocks such as limestone, dolostone, marble, granite, basalt, conglomerate, tuff, and shale can be transformed into skarn by metasomatism [64–66]. Skarns can form on both sides of a contact between a magma body and its surrounding rock [64–66].

Those formed on igneous side of the contact are known as endoskarns, while those formed on the country-rock side of the contact are known as exoskarns [64–66]. In this study, we provide the characteristics of formation of such a metasomatized zone (exoskarn) developed at the contact between the intruded lamprophyre dyke and the dolomitic marble. We have not observed any effect of a reverse process in the outcrop, with the fluids entering the hot lamprophyre dyke and metasomatizing it. Our petrographic observation shows that most of the biotite and amphibole have not undergone any alterations/dehydration due to inflow of CO_2 from the country rocks to dyke. The Ca and Mg (main elements in the marble) bearing CO_2 expulsion towards the dyke could have generated dry minerals by dehydration of amphibole/biotite in the dyke because of the high volume of CO_2 in the marble. However, such alterations are not observed in the lamprophyre dyke.

In our example, the lamprophyre dyke intruded the marble producing the development of the metasomatized marble zone characterized by olivine, serpentine, biotite, spinel, calcite, dolomite, and hematite. As the intruding magma cools down, it releases heat and fluid. Fluid expelled from the magma acts like a solvent that might have ability to dissolve and re-precipitate new minerals in the neighboring rocks [67,68]. Fluid released from the crystallizing intrusion infiltrates through interconnected fracture networks, pores, and along mineral grain boundaries [15,16,61–64,68]. Equation (1) shows that the olivine and calcite-bearing metasomatized marble region could be formed by the infiltration of silica-saturated fluid that dissolved existing dolomite in the marble. Our phase diagram result, in the first run, suggests that olivine, diopside, dolomite, calcite, and CO_2 are stable in the bulk chemistry of the metasomatized marble, where the dolomite to calcite transition occurs above 500 to 650 °C (Figure 9a). However, this result could not generate all the minerals observed in the metasomatized marble, such as biotite, spinel, and hematite.

Our detailed observations revealed that hematite acts as a major oxide mineral in the metasomatized marble. Serpentine pods bearing resorbed olivine have an oxidation rim of hematite around them. This rim could have formed initially on olivine grain boundaries before serpentinization occurred. The formation of the rim could be represented by the following reaction:

$$2\ Fe_2SiO_4\ (olivine) + O_2 = 2\ Fe_2O_3\ (hematite) + 2\ SiO_2. \tag{5}$$
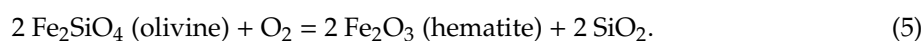
We have not observed any graphite in the metasomatized marble, where the presence of graphite would represent reduced conditions. For these reasons, we calculated the new pseudosection at an oxygen fugacity of ~log fO_2 = −14 (magnetite to hematite transition at 600–800 °C) [56] in the second run. Our new calculations show that biotite and spinel is stable at a high temperature with a high oxygen fugacity (Figure 9b). The comparison of the mineral chemistry data of the olivine and spinel with that of the isopleths for them in the P-T conditions indicates that the olivine, biotite, calcite, spinel and diopside assemblage could be formed at ~750 °C and 130 MPa. Spinel is absent, and anorthite is stable beyond this pressure. Serpentine is stable towards the low temperature side (Figure 9b). Serpentine formation can be explained by the increase in water activity due to the escape of exsolved CO_2 at low temperature or the influx of a second round of water from the cooling dyke.

If the dolomite was dissolved by the infiltration of silica saturated fluid, diopside should have formed prior to olivine (Figure 9). Previous studies on the variation in SiO_2 vs. CO_2 activity have expected the formation of diopside + calcite by Equation (2) earlier than olivine + calcite forms by Equation (1) [13]. They also predict approximately 10 times more diopside-bearing rock than the current assemblage. Their model fluid flow also suggests that olivine + calcite forms only if the silica in the initial fluid has been removed after formation of diopside by Equation (2) upstream. Our sample has stable biotite formed along with the olivine, spinel and calcite assemblage. The effect of the K concentration on the stability of clinopyroxene is observed in the experiments on granodioritic rocks [57,58]. Therefore, we considered the effect of K activity on the stability of minerals in our third pseudosection calculation. In this attempt, K_2O is considered as an independent mobile component in the system. Our result suggests that at ~750 °C and 130 MPa, the biotite-bearing olivine, spinel, and calcite assemblage is stable above log a_{K2O}~40 (Figure 10). The diopside-bearing assemblage is

stable below this activity. The result suggests that K_2O activity instead of SiO_2 has a major role in destabilizing diopside in the silica-saturated infiltrating fluid.

Our geochemical data and Gresens analysis using the isocon method show that major elements such as SiO_2, FeO, and a minor amount of K_2O are mostly infiltrated from the fluid expelled from the lamprophyre dyke (Figures 7 and 11). No/minor addition of CaO or MgO occurred in the metasomatized marble compared to the normal marble. The presence of hematite and biotite shows that infiltrating fluid was relatively oxidizing. LREEs, U, Th, and Sr are the main trace elements highly dissolved in the infiltrating fluid (Figures 8 and 11). HREEs show enrichment and a flat pattern comparable to the dolomitic marble. Most of the other trace elements show no particular enrichment in the metasomatized marble. However, Zr, V, Cr, Y, and Ba show a slight enrichment (Figure 11). Our example shows that Si, Fe, K, Sr, U, Th, and REEs are highly mobile during the infiltration metasomatic event (Figures 8 and 11).

In the metasomatized marble, fluid infiltration occurs along mineral grain boundaries, through fracture networks in the dolomite, and by generating nano-scale porosity in the dolomite. Depending on the existing pressure-temperature conditions, dissolved chemical components in the fluid eventually get saturated and precipitate new minerals [68]. This process would last until an equilibrium established between minerals and fluid composition [68]. This study is an example of geochemical and thermodynamic changes that might happen during metasomatic processes at a local scale. Many such studies explain how the breakdown or dissolution of carbonate assemblages occurs in skarn deposits, calcareous sandstones, and many hydrothermally altered rocks [15–17,61–64,68]. In this study, we have shown the importance of K activity in the infiltrating fluid, which could control the mineralogy of the metasomatized marble. Experimental studies show that CO_2 solubility is highly dependent on various cations, such as Ca, Na, and K, in the fluid/melt [69–71]. Although much is understood about fluid occurrence in the absence of high P-T constraints [70,71], we mainly extrapolate fluid properties at more familiar low-pressure conditions to study the implications of such process in a regional-scale (lower crust/mantle) metasomatism [71,72]. In a regional scale, fluid–rock interactions play an important role in the evolution and properties of the crust/mantle [3–6]. A high abundance of C-bearing phases in mantle is obvious from studies of mantle xenoliths, carbonatites, nephelinites, and melilitites [72–75]. Our study is important in further expanding our knowledge about the capacity of solute-bearing H_2O-CO_2 fluids to change the geochemistry and mineralogy of the rocks that they are in contact with. Our example shows that Si, Fe, K, Y, V, Sr, Nb, U, Th, and REEs are highly mobile in such fluids. Most of these elements are main components of exploring geochemical evolution of rocks in crust/mantle. The middle crust is composed of rocks at amphibolite facies P-T conditions with a granodioritic bulk composition containing significant amounts of K, Th, and U [8]. The results from this study will help us to understand the possible regional effects of such fluid interactions during crustal/mantle interactions.

7. Conclusions

(1) The intrusion of the hot lamprophyre dyke into the dolomitic marble generated the metasomatized marble zone containing an olivine, serpentine, biotite, spinel, dolomite, calcite. and hematite assemblage.

(2) Fluid infiltration is the main cause of metasomatic alteration in the dolomitic marble at ~750 °C/ 130 MPa.

(3) The fluid composition was mainly CO_2, with minor H_2O, Cl, and F during the initial stage. As the dyke cooled and crystallized, water released from the dyke serpentinized the assemblages that were formed during the initial stage.

(4) If the dolomite was dissolved by the infiltration of silica saturated fluid, diopside should have formed first instead of olivine. Our log activity (K_2O)-temperature pseudosection shows that K activity in the infiltrating fluid caused the absence of diopside in the metasomatized marble at a log activity (a_{K2O}) ~−40.

(5) Si, Fe, K, Y, Sr, Nb, U, Th, and REEs are highly mobile in the infiltrating H_2O-CO_2 fluid.

References

1. Zharikov, V.A.; Pertsev, N.N.; Rusinov, V.L.; Callegari, E.; Fettes, D.J. Metasomatism and metasomatic rocks. In *A Classification of Metamorphic Rocks and Glossary of Terms*; Recommendations of the International Union of Geological Sciences Subcommission on the Systaematics of Metamorphic Rocks; IUGS: Paris, France, 2007.

2. Plumper, O.; Botan, A.; Los, C.; Liu, Y.; Malthe-Sørenssen, A.; Jamtveit, B. Fluid-driven metamorphism of the continental crust governed by nanoscale fluid flow. *Nat. Geosci.* **2017**, *10*, 685–690. [CrossRef]

3. Beinlich, A.; John, T.; Vrijmoed, J.C.; Tominaga, M.; Magna, T.; Podladchikov, Y.Y. Instantaneous rock transformations in the deep crust driven by reactive fluid flow. *Nat. Geosci.* **2020**, *13*, 307–311. [CrossRef]

4. O'Reilly, S.; Griffin, W. Mantle metasomatism. In *Metasomatism and the Chemical Transformation of Rock: Rock-Mineral-Fluid Interaction in Terrestrial and Extraterrestrial Environments*; Harlov, D.E., Austrheim, H., Eds.; Springer: Berlin/Heidelberg, Germany, 2012.

5. Yardley, B.W.D. The role of water in crustal evolution. *J. Geol. Soc. Lond.* **2009**, *166*, 585–600. [CrossRef]

6. Touret, J.L.R.; Santosh, M.; Huizenga, J.M. High-temperature granulites and supercontinents. *Geosci. Front.* **2016**, *7*, 101–113. [CrossRef]

7. Yardley, B.W.D. Metal concentrations in crustal fluids and their relationship to ore formation. *Econ. Geol.* **2005**, *100*, 613–632. [CrossRef]

8. Jamtveit, B.; Austrheim, H.; Putnis, A. Disequilibrium metamorphism of stressed lithosphere. *Earth Sci. Rev.* **2016**, *154*, 1–13. [CrossRef]

9. Korzhinskii, D.S. *Physicochemical Basis of the Analysis of the Paragenesis of Minerals*; Consultants Bureau: New York, NY, USA, 1958.

10. Korzhinskii, D.S. *Theory of Metasomatic Zoning*; Oxford University Press: Oxford, UK, 1970.

11. Manning, C.E. Fluids of the lower crust: Deep is different. *Annu. Rev. Earth Planet. Sci.* **2018**, *46*, 67–97. [CrossRef]

12. Yardley, B.W.D. The Chemical Composition of Metasomatic Fluids in the Crust. In *Metasomatism and the Chemical Transformation of Rock: Rock-Mineral-Fluid Interaction in Terrestrial and Extraterrestrial Environments*; Harlov, D.E., Austrheim, H., Eds.; Springer: Berlin, Germany, 2012.

13. Ferry, J.M.; Ushikubo, T.; Valley, J.W. Formation of Forsterite by Silicification of Dolomite during Contact Metamorphism. *J. Petrol.* **2011**, *52*, 1619–1640. [CrossRef]

14. Bucher-Nurminen, K. The formation of the metasomatic reaction veins in dolomitic marble roof pendants in the Bergell intrusion (Province Sondrio, northern Italy). *Am. J. Sci.* **1981**, *281*, 1197–1222. [CrossRef]

15. Thompson, A.B. Calc-silicate diffusion zones between marble and pelitic schist. *J. Petrol.* **1975**, *16*, 314–346.

16. Fukuyama, M.; Nishiyama, T.; Urata, K.; Mori, Y. Steady-diffusion modelling of a reaction zone between a metamorphosed basic dyke and a marble from Hirao-dai, Fukuoka, Japan. *J. Metamorph. Geol.* **2006**, *24*, 153–168. [CrossRef]

17. Zucchi, M. Faults controlling geothermal fluid flow in low permeability rock volumes: An example from the exhumed geothermal system of eastern Elba Island (northern Tyrrhenian Sea, Italy). *Geothermics* **2020**, *85*, 101765. [CrossRef]

18. Bucher-Nurminen, K. On the mechanism of contact metamorphic aureole formation in dolomitic country rock by the Adamello intrusion (northern Italy). *Am. Mineral.* **1982**, *67*, 1101–1117.

19. Bucher, K. Growth mechanisms of metasomatic reaction veins in dolomite marbles from the Bergell Alps. *Mineral. Petrol.* **1998**, *63*, 151–171. [CrossRef]

20. Holness, M.B. Fluid flow paths and mechanisms of fluid infiltration in carbonates during contact metamorphism: The Beinn an Dubhaich aureole, Skye. *J. Metamorph. Geol.* **1997**, *15*, 59–70. [CrossRef]

21. Bowen, N.L. Progressive metamorphism of siliceous limestone and dolomite. *J. Geol.* **1940**, *48*, 225–274. [CrossRef]

22. Skippen, G.B. An experimental model for low pressure metamorphism of siliceous dolomite marble. *Am. J. Sci.* **1974**, *274*, 487–509. [CrossRef]

23. Moore, J.N.; Kerrick, D.M. Equilibria in siliceous dolomites of the Alta aureole. *Utah. Am. J. Sci.* **1976**, *276*, 502–524. [CrossRef]

24. Ferry, J.M. Role of fluid flow in the contact metamorphism of siliceous dolomitic limestones. *Am. Mineral.* **1994**, *79*, 719–736.

25. Roselle, G.T. Integrated Petrologic, Stable Isotopic, and Statistical Study of Fluid-Flow in Carbonates of the Ubehebe Peak Contact Aureole, Death Valley National Park, California. Ph.D. Thesis, University of Wisconsin, Madison, WI, USA, 1997.

26. Cook, S.J.; Bowman, J.R. Mineralogical evidence for fluid-rock interaction accompanying prograde contact metamorphism of siliceous dolomites: Alta aureole, Utah, USA. *J. Petrol.* **2000**, *41*, 739–757. [CrossRef]

27. Muller, T.; Baumgartner, L.P.; Foster, C.T., Jr.; Vennemann, T.W. Metastable prograde mineral reactions in contact aureoles. *Geology* **2004**, *32*, 821–824. [CrossRef]

28. Ferry, J.M. Calcite inclusions in forsterite. *Am. Mineral.* **2001**, *86*, 773–779. [CrossRef]

29. Cho, M.; Lee, Y.; Kim, T.; Cheong, W.; Kim, Y.; Lee, S.R. Tectonic evolution of Precambrian basement massifs and an adjoining fold-and-thrust belt (Gyeonggi Marginal Belt), Korea: An overview. *Geosci. J.* **2017**, *21*, 845–865. [CrossRef]

30. Kim, S.W.; Kwon, S.; Santosh, M.; Cho, D.L.; Kee, W.S.; Lee, S.B.; Jeong, Y.J. Detrital zircon U-Pb and Hf isotope characteristics of the Early Neoproterozoic successions in the central-western Korean Peninsula: Implication for the Precambrian tectonic history of East Asia. *Precambrian Res.* **2019**, *322*, 24–41. [CrossRef]

31. Kwon, S.; Sajeev, K.; Mitra, G.; Park, Y.; Kim, S.W.; Ryu, I.-C. Evidence for Permo-Triassic collision on Far East Asia: The Korean collisional orogen. *Earth Planet. Sci. Lett.* **2009**, *279*, 340–349. [CrossRef]

32. Kwon, S.; Kim, S.W.; Santosh, M. Multiple generations of mafic–ultramafic rocks from the Hongseong suture zone,western South Korea: Implications for the geodynamic evolution of NE Asia. *Lithos* **2013**, *161*, 68–83. [CrossRef]

33. Sajeev, K.; Jeong, J.; Kwon, S.; Kee, W.-S.; Kim, S.W.; Komiya, T.; Itaya, T.; Jung, H.-S.; Park, Y. High P-T granulite relicts from the Imjingang Belt, South Korea: Tectonic significance. *Gondwana Res.* **2010**, *17*, 75–86. [CrossRef]

34. Kim, S.W.; Kwon, S.; Park, S.-I.; Yi, K.; Santosh, M. Early to Middle Paleozoic tectonometamorphic evolution of the Hongseong area, central western Korean Peninsula: Tectonic implications. *Gondwana Res.* **2017**, *47*, 308–322. [CrossRef]

35. Kim, S.W.; Park, S.-I.; Jang, Y.; Kwon, S.; Kim, S.J.; Santosh, M. Tracking Paleozoic evolution of the South Korean Peninsula from detrital zircon records: Implications for the tectonic history of east Asia. *Gondwana Res.* **2017**, *50*, 195–215. [CrossRef]

36. Park, S.-I.; Kim, S.W.; Kwon, S.; Santosh, M.; Ko, K.; Kee, W.-S. Nature of Late Mesoproterozoic to Middle Neoproterozoic magmatism in the western Gyeonggi massif, Korean Peninsula and its tectonic significance. *Gondwana Res.* **2017**, *47*, 291–307. [CrossRef]

37. Kim, S.W.; Cho, D.-L.; Lee, S.-B.; Kwon, S.; Park, S.-I.; Santosh, M.; Kee, W.-S. Mesoproterozoic magmatic suites from the central-western Korean Peninsula: Imprints of Columbia disruption in East Asia. *Precambrian Res.* **2018**, *306*, 155–173. [CrossRef]

38. Jang, Y.; Kwon, S.; Song, Y.; Kim, S.W.; Kwon, Y.K.; Yi, K. Phanerozoic polyphase orogenies recorded in the northeastern Okcheon Belt, Korea from SHRIMP U-Pb detrital zircon and K-Ar illite geochronologies. *J. Asian Earth Sci.* **2018**, *157*, 198–217. [CrossRef]

39. Park, S.-I.; Kwon, S.; Kim, S.W.; Hong, P.S.; Santosh, M. A Mesozoic orogenic cycle from post-collision to subduction in the southwestern Korean Peninsula: New structural, geochemical, and chronological evidence. *J. Asian Earth Sci.* **2018**, *157*, 166–188. [CrossRef]

40. Kim, H.S.; Kwon, S.; Kim, S.W.; Santosh, M. Permo-Triassic high-pressure metamorphism in the central western Korean Peninsula, and its link to Paleo-Tethyan Ocean closure: Key issues revisited. *Geosci. Front.* **2018**, *9*, 1325–1335. [CrossRef]

41. Santosh, M.; Hu, C.N.; Kim, S.W.; Tang, L.; Kee, W.S. Late Paleoproterozoic ultrahigh-temperature metamorphism in the Korean Peninsula. *Precambrian Res.* **2018**, *308*, 111–125. [CrossRef]

42. Park, S.-I.; Noh, J.; Cheong, H.J.; Kwon, S.; Song, Y.; Kim, S.W.; Santosh, M. Inversion of two-phase extensional basin systems during subduction of the Paleo-Pacific Plate in the SW Korean Peninsula: Implication for the Mesozoic "Laramide-style" orogeny along East Asian continental margin. *Geosci. Front.* **2019**, *10*, 909–925. [CrossRef]

43. Choi, S.-J.; Kim, B.; Gihm, Y.S.; Kwon, S. Coastal landscape evolution tracked from late Holocene wave-cut benches in the Sinan Archipelago, Southwest Korea. *Geosci. Front.* **2020**, *11*, 293–301. [CrossRef]

44. Heo, C.H.; Yun, S.T.; So, C.S.; Choi, S.G. Geochemistry of the Granitoids hosting the Seolhwa Au mine, Asan district, Chungcheongnamdo province, Korea: Genetic implication on the mesothermal gold mineralization. *Geosyst. Eng.* **2002**, *5*, 54–66. [CrossRef]

45. Scarrow, J.H.; Molina, J.F.; Bea, F.; Montero, P.; Vaughan, A.P.M. Lamprophyre dikes as tectonic markers of late orogenic transtension timing and kinematics: A case study from the Central Iberian Zone. *Tectonics* **2011**, *30*, TC4007. [CrossRef]

46. Holness, M.B. Geochemical self-organization of olivine- grade contact-metamorphosed chert nodules in dolomite marble, Kilchrist, Skye. *J. Metamorph. Geol.* **1997**, *15*, 765–776. [CrossRef]

47. Pyle, J.M.; Spear, F.S.; Wark, D.A. Electron Microprobe Analysis of REE in Apatite, Monazite and Xenotime: Protocols and Pitfalls. *Rev. Mineral. Geochem.* **2002**, *48*, 337–362. [CrossRef]

48. McDonough, W.F.; Sun, S.; Ringwood, A.E.; Jagoutz, E.; Hofmann, A.W. K, Rb, and Cs in the earth and moon and the evolution of the earth's mantle. *Geochim. Cosmochim. Acta* **1992**, *56*, 1001–1012. [CrossRef]

49. Connolly, J.A.D. Multivariable phase diagrams—An algorithm based on generalized thermodynamics. *Am. J. Sci.* **1990**, *290*, 666–718. [CrossRef]

50. Connolly, J.A.D. Computation of phase equilibria by linear programming: A tool for geodynamic modeling and its application to subduction zone decarbonation. *Earth Planet. Sci. Lett.* **2005**, *236*, 524–541. [CrossRef]

51. Connolly, J.A.D. The geodynamic equation of state: What and how. *Geochem. Geophys. Geosyst.* **2009**, *10*, Q10014. [CrossRef]

52. Holland, T.J.B.; Powell, R. An internally-consistent thermodynamic dataset for phases of petrological interest. *J. Metamorph. Geol.* **1998**, *16*, 309–344. [CrossRef]

53. Holland, T.J.B.; Powell, R. A compensated-Redlich-Kwong(CORK) equation for volumes and fugacities of CO_2 and H_2O in the range 1 bar to 50 kbar and 100–1600 °C. *Contrib. Mineral Petrol.* **1991**, *109*, 265–273. [CrossRef]

54. Anovitz, L.; Essene, E.J. Phase equilibria in the system $CaCO_3$-$MgCO_3$-$FeCO_3$. *J. Petrol.* **1987**, *28*, 389–414. [CrossRef]

55. Tajcmanova, L.; Connolly, J.A.D.; Cesare, B. A thermodynamic model for titanium and ferric iron solution in biotite. *J. Metamorph. Geol.* **2009**, *27*, 153–164. [CrossRef]

56. Frost, B.R. Introduction to oxygen fugacity and its petrologic importance. In *Oxide Minerals: Petrologic and Magnetic Significance*; Lindsley, D.H., Ed.; Reviews in Mineralogy; Mineralogical Society of America: Chantilly, VA, USA, 1991; Volume 25, pp. 1–9.

57. Safonov, O.G.; Aranovich, L.Y. Alkali control of high-grade metamorphism and granitization. *Geosci. Front.* **2014**, *5*, 711–727. [CrossRef]

58. Safonov, O.G.; Kosova, S.A.; Van Reenen, D.D. Interaction of biotite–amphibole gneiss with H2O–CO2–(K,Na)Cl fluids at 550 MPa and 750 and 800 °C : Experimental study and applications to dehydration and partial melting in the middle crust. *J. Petrol.* **2014**, *12*, 2419–2456. [CrossRef]

59. Grant, J.A. The isocon diagram-A simple solution to Gresens equation for metasomatic alteration. *Econ. Geol.* **1986**, *81*, 1976–1982. [CrossRef]

60. Gresens, R.L. Composition-volume relationships of metasomatism. *Chem. Geol.* **1967**, *2*, 47–55. [CrossRef]

61. Ducoux, M.; Branquet, Y.; Jolivet, L.; Arbaret, L.; Grasemann, B.; Rabillard, A.; Gumiaux, C.; Drufin, S. Syn-kinematic skarns and fluid drainage along detachments: The West Cycladic Detachment System on Serifos Island (Cyclades, Greece) and its related mineralization. *Tectonophysics* **2017**, *695*, 1–26. [CrossRef]

62. Zucchi, M.; Brogi, A.; Liotta, D.; Rimondi, V.; Ruggieri, G.; Montegrossi, G.; Caggianelli, A.; Dini, A. Permeability and hydraulic conductivity of faulted micaschist in the eastern Elba Island exhumed geothermal system (Tyrrhenian sea, Italy): Insights from Cala Stagnone. *Geothermics* **2017**, *70*, 125–145. [CrossRef]

63. Liotta, D.; Brogi, A.; Ruggieri, G.; Rimondi, V.; Zucchi, M.; Helgadóttir, H.M.; Montegrossi, G.; Friðleifsson, G.O. Fracture analysis, hydrothermal mineralization and fluid pathways in the Neogene Geitafell central volcano: Insights for the Krafla active geothermal system, Iceland. *J. Volcanol. Geotherm. Res.* **2018**, *391*, 106502. [CrossRef]

64. Einaudi, M.T.; Meinert, L.D.; Newberry, R.J. Skarn deposits. *Econ. Geol.* **1981**, *100*, 317–391.

65. Meinert, L.D. Skarn and skarn deposits. *Geosci. Can.* **1992**, *19*, 145–162.

66. Meinert, L.D.; Dipple, G.M.; Nicolescu, S. *World Skarn Deposits*; Economic Geology 100th Anniversary Volume; Society of Economic Geologists, Inc.: Littleton, CO, USA, 2005; pp. 299–336.

67. Beinlich, A.; Barker, S.L.L.; Dipple, G.M.; Hansen, L.D.; Megaw, P.K.M. Large-Scale Stable Isotope Alteration Around the Hydrothermal Carbonate-Replacement Cinco de Mayo Zn-Ag Deposit, Mexico. *Econ. Geol.* **2019**, *114*, 375–396. [CrossRef]

68. Putnis, A. Mineral replacement reactions. *Rev. Mineral. Geochem.* **2009**, *70*, 87–124. [CrossRef]

69. Meinert, L.D.; Hefton, K.K.; Mayes, D.; Tasiran, I. Geology, zonation, and fluid evolution of the Big Gossan Cu-Au skarn deposit, Ertsberg district, Irian Jaya. *Econ. Geol.* **1997**, *92*, 509–526. [CrossRef]

70. Brooker, R.A.; Blank, J.G. Experimental Studies of Carbon Dioxide in Silicate Melts: Solubility, Speciation, and Stable Carbon Isotope Behavior. In *Volatiles in Magmas*; Carroll, M.R., Holloway, S.R., Eds.; Mineralogical Society of America: Chantilly, VA, USA, 1994; pp. 157–186.

71. Holloway, J.R.; Blank, J.G. Application of experimental results to C-O-H species in natural melts. *Rev. Mineral. Geochem.* **1994**, *30*, 187–230.

72. Brey., G.P. Origin of olivine melilitites—Chemical and experimental constraints. *J. Volcanol. Geotherm. Res.* **1978**, *3*, 61–88. [CrossRef]

73. Fogel, R.A.; Rutherford, M.J. The solubility of carbon dioxide in rhyolitic melts; A quantitative FTIR study. *Am. Mineral.* **1990**, *75*, 1311–1326.

74. Bailey, D.K.; Macdonald, R. Dry Peralkaline Felsic Liquids and Carbon Dioxide Flux through the Kenya Rift Zone. In *Magmatic Processes: Physiochemical Principles*; Special Publication No. 1; Mysen, B.O., Ed.; Geochemical Society: Washington, DC, USA, 1987; pp. 91–105.

75. Haggerty, S.E. A diamond trilogy; superplumes, supercontinents, and supernovae. *Science* **1999**, *285*, 851–860. [CrossRef]